



ARCHIVES of FOUNDRY ENGINEERING

10.24425/afe.2025.153773


Published quarterly as the organ of the Foundry Commission of the Polish Academy of Sciences

ISSN (2299-2944)
Volume 2025
Issue 1/2025

43 – 51

6/1

Thermodynamic Analysis and Impact of Quenching on Microstructure & Mechanical Properties of High Silicon Ductile Iron

B. David Joseph ^{a,*} , B. Pustal ^a, T. Weirich ^b, A. Bührig-Polaczek ^a^a Foundry Institute, RWTH Aachen, Germany^b Central Facility for Electron Microscopy, RWTH Aachen, Germany

* Corresponding author: E-mail address: b.david-joseph@gi.rwth-aachen.de

Received 29.07.2024; accepted in revised form 15.11.2024; available online 17.03.2025

Abstract

Solid-solution-strengthened ferritic ductile iron (SSFDI) exhibits superior tensile strength to elongation ratios up to a critical silicon content of 4.3 wt.%. Beyond this threshold, this material experiences a sudden drop in ultimate tensile strength and elongation at breakage. Previous studies indicate that this may be because of the formation of superstructures like B2 and D03 especially at regions with high silicon content. This study aims to comprehend thermodynamics behind phase transition during solid-state transformation in high silicon ductile iron. Using thermodynamic simulations, this current investigation tries to pinpoint the transition temperature from the ferritic phase to superstructure formation especially B2 superstructure. Additionally, analysis is made to see consequences of quenching above this transition temperature on microstructure, and mechanical properties.

The results contribute insights into phase transitions in high silicon ductile iron, offering practical guidance for optimizing heat treatment processes. By isolating the transition temperature and evaluating the impact of quenching, we provide actionable strategies for controlling microstructural evolution and enhancing mechanical performance in SSFDI.

In conclusion, this research represents a crucial advancement in realizing the full potential of high silicon ductile iron for engineering applications. The findings deepen our understanding of the material's behavior and furnish practical approaches for improving its mechanical properties through controlled heat treatments and quenching processes.

Keywords: Ductile iron, Silicon superstructures, Thermodynamics, Quenching, Impact energy

1. Introduction

High silicon ductile iron offers significant advantages over conventional ductile cast iron due to its enhanced strength and remarkable elongation at fracture, achieved through solid solution strengthening [1]. Additionally, the fully ferritic metal matrix of high silicon ductile iron improves machinability, making it more suitable for various industrial applications like automobile and

wind turbine where both performance and ease of processing are critical [2].

The addition of silicon to cast iron alloys has been recognized for its substantial impact on material properties. Pioneering research by White et al. identified how increased silicon content, specifically from approximately 4 to 5 wt%, could significantly enhance solid solution strengthening [3]. This enhancement allowed for the achievement of exceptional strength alongside remarkable elongation at fracture. Silicon's influence extends to altering the eutectic and eutectoid temperatures within the stable



© The Author(s) 2025. Open Access. This article is licensed under a Creative Commons Attribution 4.0 International License (<http://creativecommons.org/licenses/by/4.0/>), which permits use, sharing, adaptation, distribution and reproduction in any medium or format, as long as you give appropriate credit to the original author(s) and the source, provide a link to the Creative Commons licence, and indicate if changes were made.

iron-graphite system, positioning it as a key graphitizing alloying element [4].

Building on this foundational research, advancements in the field led to the development of novel solid-solution-strengthened grades of spheroidal graphite iron (SGI). Notable among these are EN-GJS-450-18 with 3.2 wt% silicon, EN-GJS-500-14 with 3.8 wt% silicon, and EN-GJS-600-10 with 4.3 wt% silicon [5]. These innovative grades were formally incorporated into the European standard DIN EN 1563 in 2012, marking a significant milestone in the application of silicon-based alloying elements to produce high-strength cast iron materials. The recognition of these new grades underscored their remarkable mechanical properties and performance advantages in various industrial applications[6].

Despite these advantages, challenges arise with silicon alloying. Research has indicated a practical limit to the maximum silicon content, typically around 4.3 wt% [7]. Beyond this threshold, mechanical properties rapidly decline, with elongation at fracture diminishing to nearly 0%. This finding highlights the need to carefully optimize silicon content to balance strengthening effects with acceptable ductility levels in cast iron materials[2].

The decline in mechanical properties is attributed mainly to the formation of iron-silicon long-range orderings, observed in high-silicon steels. These orderings, manifesting as B2- and DO3-ordered phases, are believed to cause embrittlement at higher silicon contents [8]. Transmission electron microscopy studies have confirmed these superstructures in samples with elevated silicon levels, notably detecting B2- and DO3-superstructures in samples with silicon content as low as 3.95 wt% because of negative segregation properties of silicon [9]. This suggests embrittlement can occur even below the critical limit of 4.3 wt% silicon, emphasizing the importance of managing silicon segregation through alloying and cooling conditions. Additionally, the decoupled eutectic solidification process in ductile iron alloys leads to distinct micro segregation profiles within their microstructures. This phenomenon results from the differential behavior of various alloying elements during solidification. Negative segregating elements, such as silicon and aluminum, tend to accumulate within the solidifying austenitic crystal lattice, while elements like manganese and chromium are rejected at the solid-liquid interface, enriching the last-to-freeze zones. The selective enrichment of manganese and chromium stabilizes carbides, significantly influencing the mechanical properties and performance of ductile iron alloys [10].

In this study, we compare cast parts that undergo two different cooling processes to determine the effectiveness of quenching rates in preventing the ordering reaction in high silicon ductile cast iron. One set of cast parts is quenched in water from a defined temperature, suggested based on Thermo-Calc calculations. The other set cools to room temperature inside the furan mold. By analyzing the outcomes of these distinct cooling methods, we aim to establish whether the quenching rate is sufficient to inhibit the ordering reaction and thereby enhance the material properties of high silicon ductile cast iron.

2. Design of experiments

As this study aimed to determine the effect of quenching on the suppression of ordering reaction in high silicon ductile cast iron.

First, phase field simulations were used to study how different cooling rates, based on the size of the cast part, affect silicon segregation in an alloy with 3.4 wt.% silicon. These simulations helped identify how silicon segregates during cooling, and the results were used to find the equilibrium ordering temperatures at different silicon levels using Thermo-Calc software.

After determining the ordering temperatures, casting experiments were carried out using the alloy compositions and quenching temperatures derived from the phase field simulations and Thermo-Calc analysis. The casting setup was designed to ensure that both quenched and non-quenched samples had the same alloy compositions and pouring temperatures for consistent conditions. Following casting, the samples were examined using metallography to study their microstructure, mechanical testing to measure their mechanical properties, and transmission electron microscopy (TEM) to check for the presence of B2 superstructures. This thorough approach allowed for a detailed assessment of how quenching impacts the microstructure and mechanical properties of high silicon ductile cast iron.

2.1. Experimental procedure

The raw materials used in this experiment included recirculation material, pure iron (99.9% Fe), and ferrosilicon (FeSi75). These materials were prepared and melted using an Otto Junker medium-frequency induction furnace with a maximum capacity of 250 kg.

The melt was heated to 1500 °C and maintained at that temperature for 5 minutes to ensure homogeneity of the melt. After this period, samples were taken for spectrometer and thermal analysis to confirm that the silicon and carbon content were as expected. Upon verification of the desired silicon and carbon content, the melt underwent deslagging to remove impurities. Following deslagging, a magnesium treatment was performed using a magnesium master alloy containing 1.9 wt.% calcium. This treatment was conducted in a ladle, where the magnesium master alloy was covered with steel scrap, and the melt was poured from the furnace into the ladle. After the magnesium treatment, a second deslagging was carried out to ensure proper mold filling without clogging the filters. Inoculation was then accomplished by adding 0.3 wt.% of a bismuth- and cerium-based inoculant. Subsequently, samples for thermal and spectrometric analyses were taken, and the base cast iron was poured into molds at 1350 °C. For the casting process, a furan-bonded sand mold was used, containing four Y2 geometry (module size: 0.8 cm) in each mold, with a total of four molds utilized.

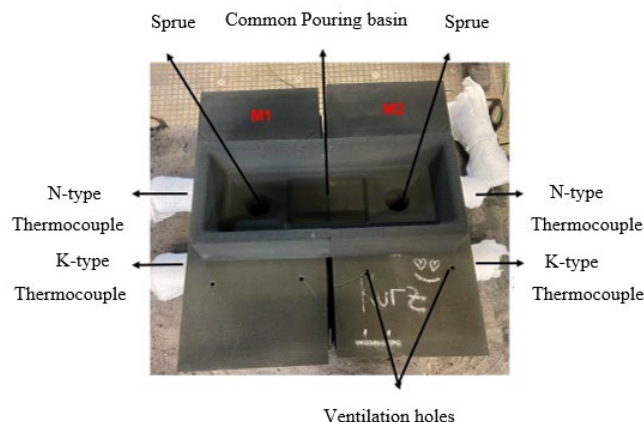


Fig. 1. Arrangement of mold 1 (M1) and mold 2 (M2) with common pouring basin and different thermocouple attachments to monitor cooling conditions

The four molds were named as M1, M2, M3, and M4. M1 and M2 were joined together with a common pouring basin as shown in Fig. 1, as were M3 and M4. During cooling, M1 and M2 were separated from each other, and M3 and M4 were also separated. The cast parts in molds M1 and M4 were broken at a certain temperature based on Thermo-Calc calculations and then subjected to water quenching, while the cast parts in molds M2 and M3 remained inside and underwent normal cooling within the furan sand mold. The common pouring basin ensured that the pouring temperature was consistent for M1 and M2 as well as M3 and M4. From each Y2 casting, tensile test specimens and Charpy specimens were machined from specific locations as indicated in Fig. 2. Additionally, samples for metallographic and electron microscopic examinations were machined from the immediate vicinity of the tensile test specimens. This thorough preparation and analysis ensured a comprehensive understanding of the quenching effects on the microstructure and mechanical properties of high silicon ductile cast iron.

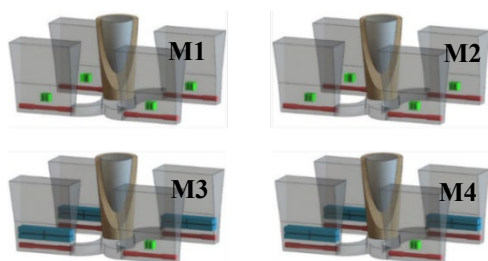


Fig. 2. Sample extraction plan from each Y2-part for tensile (red), Charpy (blue) and metallographic analysis (green)

3. Simulation procedure

Phase field simulations were conducted using MICRESS version 7.2 to analyze the influence of cooling conditions on silicon segregation in high silicon ductile cast iron [11]. MICRESS utilizes

thermodynamic and mobility databases from Thermo-Calc to predict phase evolution and dissolution, including the segregation of alloying elements. Heat extraction during both solidification and solid-state transformation was calculated based on the heat diffusibility of the mold and the modulus of the cast part. A representative volume element (RVE) of 200 micrometers was generated for these calculations. In these simulations, the dendritic growth of austenite and the faceted growth of graphite were considered. Interfacial energies between liquid, austenite, graphite, and ferrite were obtained from existing literature. The nucleation of all phases was modeled using a seed distribution function along with critical undercooling. Additionally, the seed density function was calibrated against real nodule counts derived from actual micrographs.

The Fe-Si-C phase diagram was simulated using the TCFe8 database in Thermo-Calc to investigate the thermodynamic behavior of the alloy [12] [13]. The primary objective of these simulations was to analyze the influence of silicon content on the ordering temperature. The results obtained from these simulations were then used to determine the quenching start temperature for the cast part from M1 and M4.

4. Specimen analysis

4.1. Mechanical properties

For the mechanical testing of the alloys, tensile specimens were prepared as illustrated in Fig. 2. Cylindrical cores with an 18 mm diameter were extracted from the castings using a water-cooled core drill. These cores were then machined into shape A specimens, in accordance with the DIN EN 50125 standard [14]. The final specimens had an 8 mm diameter and a total length of 115 mm. Tensile tests were conducted at a crosshead speed of 0.60 mm/min to evaluate the mechanical properties. This standardized approach ensured the reproducibility and accuracy of results, facilitating a thorough comparison of the mechanical characteristics between quenched and non-quenched high silicon ductile cast iron samples. Moreover, Charpy samples are also extracted from M3 and M4 as shown in Fig. 2, the Charpy tests are conducted under 25°C, 40°C, 60°C, 80°C, 100°C and 120°C to see the ductile to brittle transition temperatures in non-quenched and quenched samples.

4.2. Metallographic examinations

Metallographic samples were obtained from the immediate vicinity of the tensile test specimens using a water-cooled saw to cut 2 cm thick sections from the castings. These sections were then embedded in conductive embedding material for further preparation. The embedded samples underwent a rigorous grinding process with abrasive papers of 180, 320, 500, and 1000 grit, each stage lasting 2 minutes under a contact pressure of 20 N and a rate of 150 strokes per minute, with water used as the lubricant. Following grinding, a three-stage polishing process was conducted using diamond suspensions of 9 µm, 3 µm, and 0.25 µm particle sizes, with each stage polished at 25 N pressure for 3 to 4 minutes.

To find the pearlite fraction, the samples were etched using Nital reagent [15]. Subsequently, both polished and etched samples were examined using an optical light microscope for initial microstructural analysis [16]. Samples were then prepared for scanning electron microscopy (SEM) to conduct energy-dispersive X-ray spectroscopy (EDX) line scan and electron backscatter diffraction (EBSD) analysis. Additionally, after polishing with VibroMet, samples were further analyzed using transmission electron microscopy (TEM) to provide detailed insights into the superstructure reflections.

5. Results and discussions

Phase field simulations were meticulously conducted under three distinct cooling conditions, which corresponded to different and specific geometries: Y2, Y4, and Cylinder. These particular geometries are meticulously depicted in the Fig. 3, along with their respective and detailed cooling curves for the reference alloy composition that is thoroughly outlined in Table 1. In order to qualitatively and comprehensively analyze silicon segregation, 2D images were systematically extracted from the 3D Representative Volume Element (RVE) which was generated through precise phase field simulations. The detailed analysis revealed notable and significant differences in silicon segregation across the three distinct cooling conditions. Specifically, the fast cooling condition that is associated with the Y2 geometry exhibited the highest degree of silicon segregation among the three. This is clearly evidenced by the Fig. 4, which highlights and illustrates the superior and pronounced segregation levels in the Y2 geometry compared to the Y4 and Cylinder geometries. The observed differences underline the impact of cooling conditions on silicon segregation, emphasizing the critical role of cooling rate. Additionally, these findings offer valuable insights into the microstructural evolution of the alloy under varied cooling scenarios, contributing to a better understanding of the material behavior and properties. The fast cooling condition of the Y2 geometry, in particular, stands out due to its prominent silicon segregation, which may have significant implications for the mechanical properties and performance of the alloy. Overall, the comprehensive analysis underscores the intricate interplay between cooling conditions and microstructure, offering a nuanced perspective on the material science aspects of alloy processing and simulation.

Table 1.
Chemical composition of reference alloy

Sample	C [wt.-%]	Si [wt.-%]	Mg [wt.-%]	CE
Alloy 1	3.14	3.4	0.04	4.27

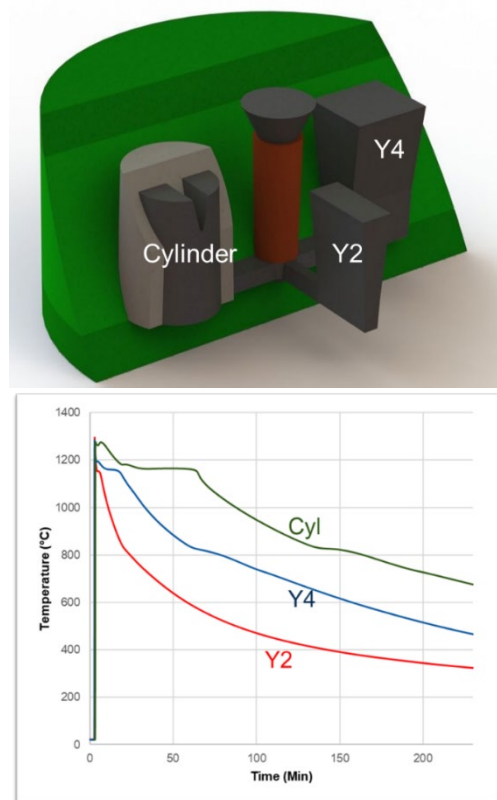


Fig. 3. Y2, Y4 and Cylinder geometries with the casting system (top) and corresponding cooling curves (bottom)

In addition to the qualitative analysis of silicon segregation, quantitative analysis was performed on the 2D section of the fast cooling (Y2) cast part using a line scan extending from the last-to-solidify region to the periphery of the graphite nodule, as shown in the Fig. 5. The graph illustrates that for the reference alloy, the maximum and minimum local silicon concentrations in the matrix phase are 3.63 wt.% and 2.7 wt.% silicon, respectively. Furthermore, another graph in the Fig. 5 presents the cumulative distribution of silicon in the entire RVE, indicating that the maximum and minimum local silicon concentrations are 0 wt.% and 3.8 wt.%. Based on this segregation profile, the alloy composition for casting is finalized as 4 wt.% Si, which is 0.2 wt.% higher than the highest silicon concentration from the cumulative distribution curve, while maintaining the carbon equivalent constant as the reference alloy.

Following the finalization of the cooling condition and alloy composition for the experimental casting based on phase field simulations, it was necessary to determine the A2-B2 ordering temperature (BCC-B2 superstructure formation temperature) under equilibrium conditions for the alloy with 2.91 wt.% C and 4 wt.% Si using Thermo-Calc simulations by changing the site fraction of sub-lattice. The Thermo-Calc results, as depicted in the Fig. 6, indicate that the ordering temperature for an alloy with 2.91 wt.% C and 4.0 wt.% Si is 442°C.

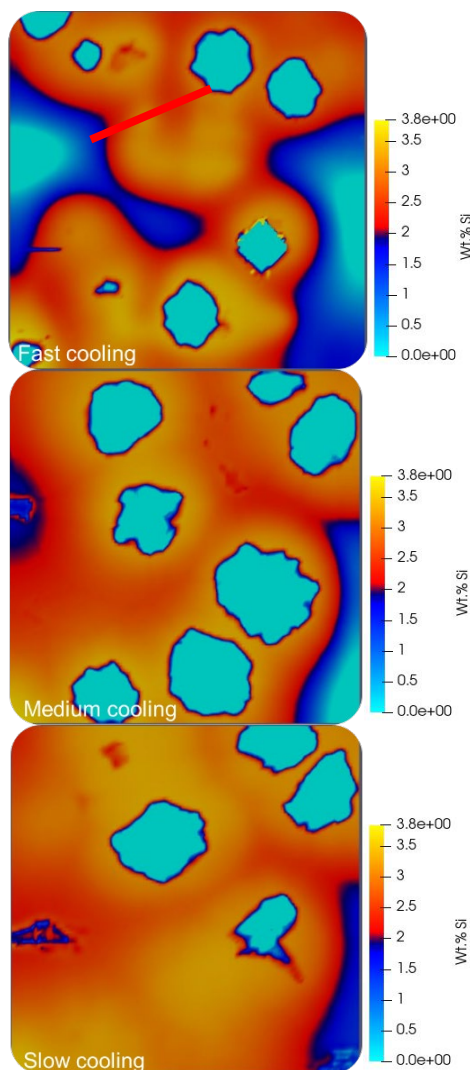


Fig. 4. 2D section from 3D RVE showing silicon segregation of reference alloy with three different cooling conditions

After confirming the alloy composition and quenching temperature for the specified alloy using phase field simulations and Thermo-Calc, experimental castings were performed. The cooling rates of all cast parts in M1, M2, M3, and M4 were measured using both N-type and K-type thermocouples. The cooling curves for M1 and M4, shown in the Fig. 7, indicate that water quenching begins at around 510°C and the quenching rate is 8.3°C/s.

Similarly, metallographic analysis was conducted to determine the nodularity and nodule count of the samples. The light microscopy images for samples from M1 (quenched) and M2 (non-quenched), shown in the Fig. 8 at a magnification of 100x, indicate that the nodularity of quenched samples is $74.7 \pm 1.62\%$, while non-quenched samples have a nodularity of $76.9 \pm 2.48\%$. The nodule count for quenched samples is $291 \pm 15 \frac{1}{mm^2}$, compared to $313 \pm 23 \frac{1}{mm^2}$ for non-quenched samples. Here the non-quenched

sample shows a slightly higher nodularity but this might be because of the location from which the image is been taken. Overall the metallographic results as expected suggests that, there is not a significant difference between the quenched and non-quenched samples in terms of nodularity and nodule count as the quenching temperature is below eutectoid.

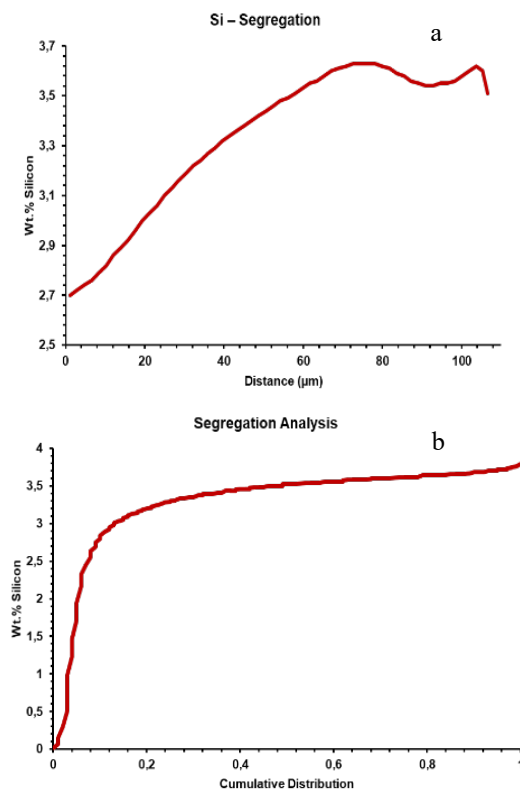


Fig. 5. Line scan on 2D section (a), silicon segregation profile corresponding to the line scan corresponding to Fig 4 (b) and cumulative distribution of silicon in the entire 3D-RVE

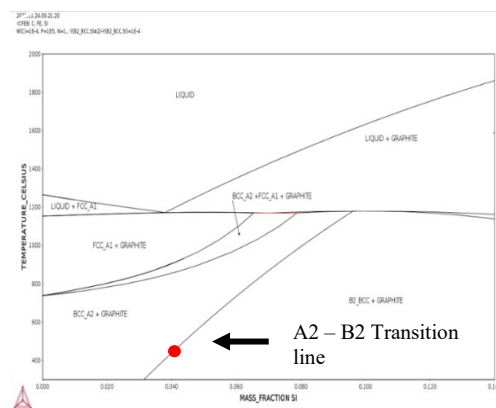


Fig. 6. Thermo-Calc results showing the ordering temperature (red dot) for alloy with 4.0wt.% Si and 2.91 wt.% C

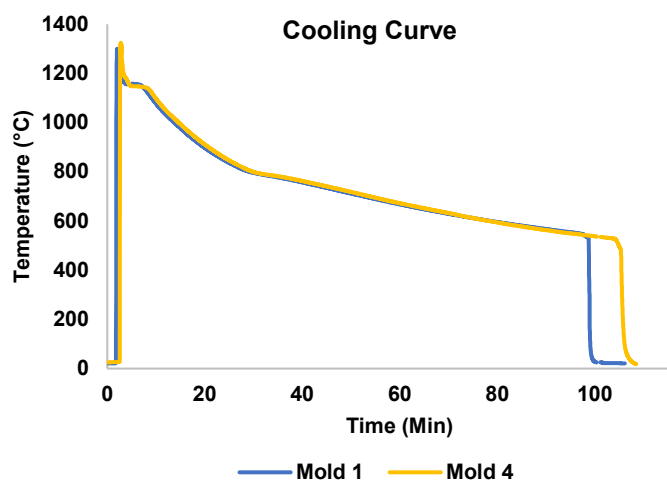


Fig. 7. Cooling curves of cast parts from molds M1 and M4

EDX line scans were performed on both non-quenched and quenched samples, and in both cases, the results did not show micro-segregation of silicon. This may be due to the length of the line scans, which ranged from 40 μm to 50 μm as line scan between close graphites could result in more homogenous distribution of silicon and moreover the line scan may not pass through a grain boundary. The line scan graphs, along with the positions of the line scans, are shown in the Fig. 9.

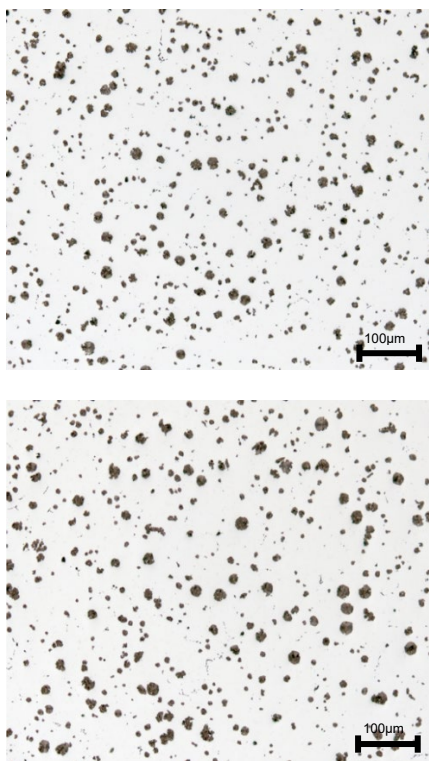


Fig. 8. Light microscopy images indicating graphite morphology of non-quenched (top) and quenched sample (bottom)

In contrast, the TEM reflections for the quenched samples also do not exhibit extra spots indicative of the B2 superstructure. Moreover, these reflections lack diffuse scattering, indicating that quenching effectively halts the diffuse scattering. This suggests that quenching could be an effective method to restrict the formation of the B2 superstructure as from the TEM it is shown for the given alloy composition the quenched sample did not show the start of ordering. The absence of B2 superstructure formation in both non-quenched and quenched samples likely explains the minimal differences observed in the metallographic and mechanical testing results between the two types of samples.

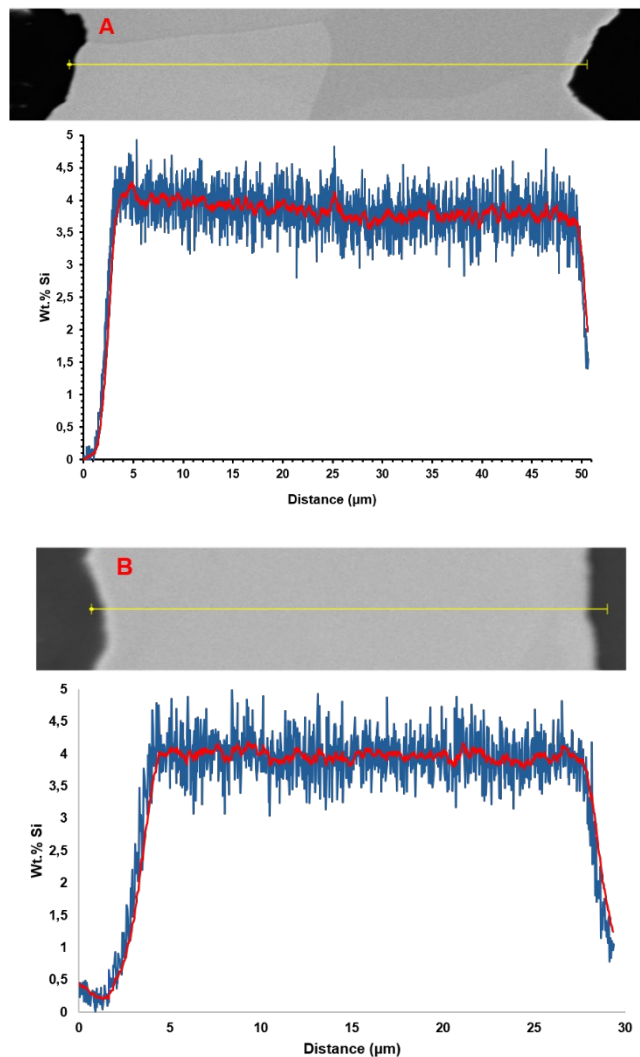


Fig. 9. EDX line scans showing segregation of silicon in non-quenched sample (A) and quenched sample (B), the location of line scan is shown above the graph

To analyze and compare the mechanical properties of the material, both tensile tests and Charpy impact tests were conducted. The tensile test results, shown in the Fig. 10, indicate that non-quenched samples exhibit slightly better ultimate tensile strength

(UTS) and elongation at break compared to quenched samples. Given the minimal differences in graphite nodularity and nodule count, it is assumed that the observed variations in mechanical properties might be attributed to thermal shock from water quenching. However, the UTS and elongation at break values for both non-quenched and quenched samples are relatively close.

Additionally, the Charpy impact test results, also shown in the Fig. 11, indicate that the brittle-to-ductile transition temperature is the same for both non-quenched and quenched samples. Therefore, based on metallographic analysis and mechanical testing, it can be concluded that quenching has no clear influence on the mechanical properties and microstructure of the material.

To further understand the influence of quenching on formation of the B2 superstructure, detailed Transmission Electron Microscopy (TEM) analysis was conducted at the Central Facility for Electron Microscopy (GFE) at RWTH Aachen University. The TEM reflections for both non-quenched and quenched samples are meticulously presented in Fig. 12 and Fig. 13, respectively.

For the non-quenched samples, the TEM reflections do not reveal any spots indicative of the B2 superstructure. However, the presence of diffuse scattering is observed, suggesting the initial stages of ordering. This observation implies that with a further increase in silicon content, the formation of the B2 superstructure is likely to occur.

Fig. 12 displays the Selected Area Electron Diffraction (SAED) pattern of the unquenched sample. The absence of weaker diffraction spots between the strong spots, as shown in the simulated overlay for the B2 structure in the bottom image, along with the presence of bright streaks from short-range diffuse scattering, proves that the phase is still locked in a non-equilibrium state.

Fig. 13 shows the SAED pattern of the quenched sample. Similar to the unquenched sample, the quenched sample remains in a non-equilibrium state, as indicated by the absence of the weaker diffraction spots that appear in the simulation overlay for the B2 structure in the bottom image. Additionally, weak spots in the experimental diffraction pattern are not compatible with either the B2 or DO3 types and are therefore thought to be due to contamination following Focused Ion Beam (FIB) sample preparation.

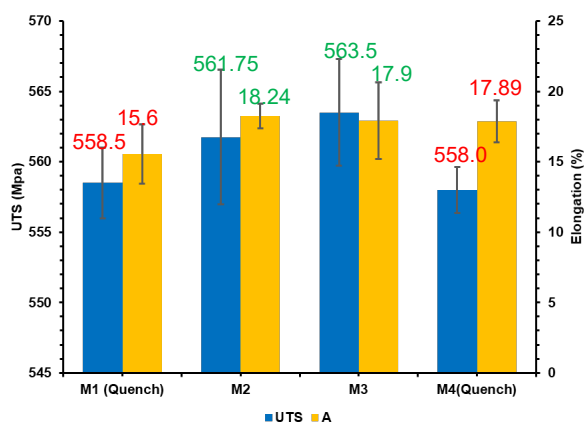


Fig. 10. Tensile test results indicating UTS and elongation at break for samples from M1, M2, M3 and M4

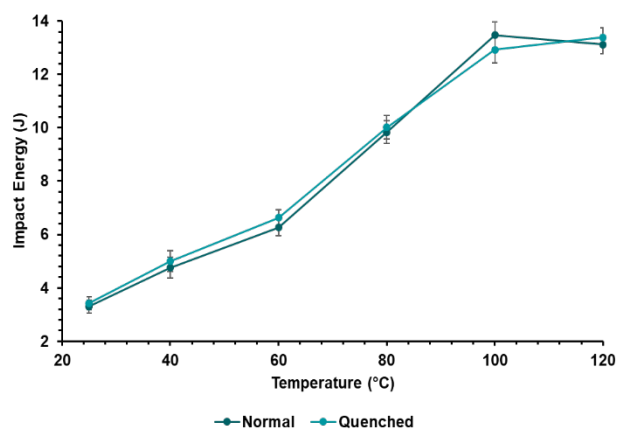


Fig. 11. Charpy test results for both non-quenched and quenched samples

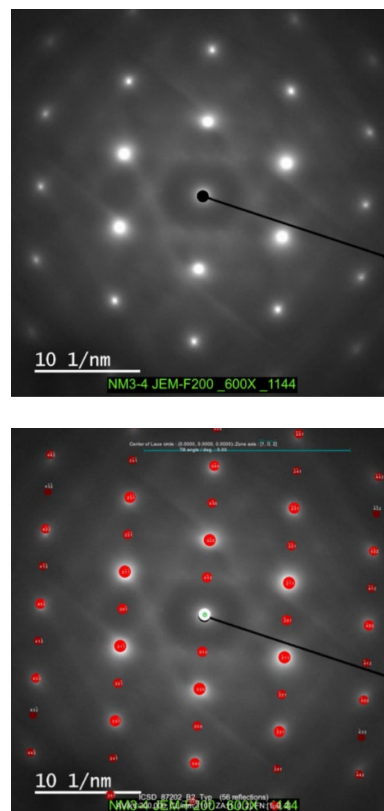


Fig. 12. Selected Area Electron Diffraction (SAED) pattern of the unquenched sample. The absence of the weaker diffraction spots between the strong spots, as shown in the simulated overlay for the B2 structure in the bottom image, and the presence of the bright streaks from (short-range) diffuse scattering prove that the phase is still locked in the non-equilibrium state

These findings provide significant insights into the microstructural behavior of the samples under different thermal conditions. They highlight the crucial role of quenching in modifying the microstructure and inhibiting the formation of the

B2 superstructure. This contributes to a better understanding of the relationship between thermal treatment and structural properties in these alloy systems. The observed non-equilibrium states in both quenched and non-quenched samples emphasize the complexity of phase transformations and the potential impact of processing conditions on material performance. This comprehensive analysis underscores the importance of precise control over thermal treatments to achieve desired material properties and microstructural stability.

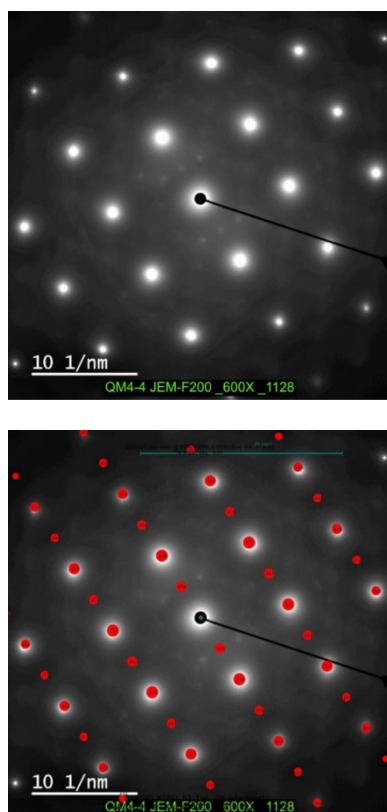


Fig. 13. Selected Area Electron Diffraction (SAED) pattern of the quenched sample. As for the unquenched sample, the sample remains in the non-equilibrium state, as indicated by the absence of the weaker diffraction spots that appear in the simulation overlay for the B2 structure in the bottom image. Additional weak spots in the experimental diffraction pattern are not compatible with either the B2 or DO₃ type and are therefore thought to be due to contamination after FIB sample preparation.

6. Conclusion

Phase field simulations were conducted under three cooling conditions corresponding to Y2, Y4, and Cylinder geometries, shown in Figure 3 with their cooling curves for the reference alloy in Table 1. Notably, the fast cooling condition in Y2 exhibited the highest silicon segregation, as illustrated in Fig. 4.

Thermo-Calc simulations determined the A2-B2 ordering temperature for the alloy with 2.91 wt.% C and 4 wt.% Si to be

442°C, depicted in Fig. 6. This informed the processing parameters to avoid undesired phases during casting.

Experimental castings were performed, and cooling rates were measured using N-type and K-type thermocouples, as shown in Fig. 7. Metallographic analysis revealed that quenched samples had a nodularity of $74.7 \pm 1.62\%$ and nodule count of 291 ± 15 , compared to $76.9 \pm 2.48\%$ nodularity and 313 ± 23 nodule count for non-quenched samples, indicating no significant difference.

EDX line scans on both non-quenched and quenched samples did not show silicon micro-segregation, likely due to the line scan lengths of 40 μm to 50 μm , as shown in Fig. 9.

Tensile tests, shown in Figure 10, indicated that non-quenched samples had slightly better UTS and elongation at break compared to quenched samples. Charpy impact tests, shown in Fig. 11, indicated similar brittle-to-ductile transition temperatures for both sample types, suggesting quenching has no clear influence on mechanical properties and microstructure.

TEM analysis, conducted at RWTH Aachen, revealed that non-quenched samples showed diffuse scattering indicative of the initial stages of ordering, while quenched samples lacked this scattering, suggesting quenching halts B2 superstructure formation (Fig. 12 and Fig. 13).

Overall, these findings highlight the impact of cooling conditions on silicon segregation, with Y2 geometry exhibiting the highest segregation under fast cooling. Thermo-Calc simulations confirmed the critical A2-B2 ordering temperature, guiding the casting process. Metallographic and mechanical testing indicated minimal differences between quenched and non-quenched samples, while TEM analysis showed that quenching at 8.3°C/s from 510°C for the given alloy effectively halts the formation of the B2 superstructure. These insights emphasize the importance of cooling rates and thermal treatments in controlling microstructural properties and performance of the alloy.

Acknowledgements

The presented results are derived from the DFG project BU1072/47-1. In addition, the authors expressed their gratitude to Dietmar Lembrecht and Ingo Braun for their contributions in preparing and performing the castings. They acknowledged the assistance of Stefanie Düker in conducting the metallographic and electron microscopy investigations and the assistance of Martina Schiffrers and Sebastian Zischke for FIB lamelle preparation and TEM analysis. The authors appreciated the valuable support provided by these individuals in the study.

References

- [1] Björkegren, L.E. (1994). *Ferritic ductile iron with higher silicon content*. Secondary Ferritic ductile iron with higher silicon content. Swedish Foundry Association (941028).
- [2] Alhussein, A., Risbet, M. & Favregeon, J. (2014). *Evolution of ferritic iron resistance through silicon content in secondary evolution of ferritic iron resistance through silicon content*.

- [3] White, W.H., Rice, L.P. & Elsea, A.R. (1951). Influence of silicon content on mechanical and high-temperature properties of nodular cast iron. Secondary Influence of Silicon Content on Mechanical and High-Temperature Properties of Nodular Cast Iron. *AFS Transactions*. 337-345.
- [4] Riebisch, M., Pustal, B. & Bührig-Polaczek, A. (2020). Impact of carbide-promoting elements on the mechanical properties of solid-solutions strengthened ductile iron. *International Journal of Metalcasting*. 14(2), 365-374. <https://doi.org/10.1007/s40962-019-00358-5>.
- [5] Deutsches Institut für Normung e.V. (2012). DIN EN 1563: Gießereiwesen - Gusseisen mit Kugelgraphit. Deutsche Fassung EN 1563:2011.
- [6] de la Torre, U., Loizaga, A., Lacaze, J. & Sertucha, J. (2014). As cast high silicon ductile irons with optimised mechanical properties and remarkable fatigue properties. *Materials Science and Technology*. 30(12), 1425-1431. <https://doi.org/10.1179/1743284713Y.000000004>.
- [7] Stets, W., Löblich, H., Gassner, G. & Schumacher, P. (2014). Solution strengthened ferritic ductile cast iron properties, production and application. *International Journal of Metalcasting*. 8, 35-40. <https://doi.org/10.1007/BF03355580>.
- [8] David Joseph, B., Alkhozai, H., Pustal, B. & Bührig-Polaczek, A. (2023). Impact of quenching and aluminium on si-segregation and B2 superstructure formation in solid solution strengthened ferritic ductile cast iron. *International Journal of Metalcasting*. 1-11. <https://doi.org/10.1007/s40962-023-01238-9>.
- [9] Weiß, P., Tekavčič, A. & Bührig-Polaczek, A. (2018). Mechanistic approach to new design concepts for high silicon ductile iron. *Materials Science and Engineering A*. 713, 67-74. <https://doi.org/10.1016/j.msea.2017.12.012>.
- [10] Hasse, S. (1996). *Duktile Gussisen: Handbuch für Gusserzeuger und Gussverwender in Secondary Duktile Gussisen: Handbuch für Gusserzeuger und Gussverwender*. Fachverlag Schiele & Schoen.
- [11] Retrieved June 10, 2024, from <https://micress.rwth-aachen.de/>
- [12] Retrieved June 10, 2024, from <https://thermocalc.com/>
- [13] Andersson, J. O., Helander, T., Höglund, L., Shi, P., & Sundman, B. (2002). Thermo-Calc and DICTRA, computational tools for material science. *Calphad*. 26(2), 273-312. [https://doi.org/10.1016/S0364-5916\(02\)00037-8](https://doi.org/10.1016/S0364-5916(02)00037-8).
- [14] Deutsches Institut für Normung e.V. (2022). DIN 50125: Prüfung metallischer Werkstoffe – Zugproben.
- [15] Beckert, M. & Klemm, H. (1962). *Handbuch der metallographischen Ätzverfahren*.
- [16] Deutsches Institut für Normung e.V. (2010). DIN EN ISO 945-1: Mikrostruktur von Gusseisen – Teil 1: Graphitklassifizierung durch visuelle Auswertung.